



Integrated reduced graphene oxide/polypyrrole hybrid aerogels for simultaneous photocatalytic decontamination and water evaporation

Shiwei Yan^a, Haojie Song^{a,*}, Yong Li^{a,*}, Jin Yang^a, Xiaohua Jia^a, Sizhe Wang^a, Xiaofei Yang^{b,*}

^a School of Materials Science & Engineering, Shaanxi Key Laboratory of Green Preparation and Functionalization for Inorganic Materials, Shaanxi University of Science & Technology, Xi'an, Shaanxi 710021, China

^b College of Science, Nanjing Forestry University, Nanjing 210037, China

ARTICLE INFO

Keywords:

Aerogels
Photocatalytic degradation
Water evaporation
Graphene
Polypyrrole

ABSTRACT

Here we report an integrated reduced graphene oxide/polypyrrole hybrid aerogel with highly efficient photodegradation performance and ultrahigh solar-powered water evaporation for simultaneous freshwater production and decontamination from complex wastewater. The nanohybrids were successfully fabricated by the combined hydrothermal reduction and freeze-drying process. The π - π interactions between two components not only prevent the stacking of reduced graphene oxide nanosheets to endow aerogels with abundant water transport channels and ideal mechanical stability, but also facilitate the interactions with organic molecules to realize high removal efficiency toward volatile organic compounds (VOCs). The wide-spectrum light harvesting, photothermal effect and solar-driven photocatalysis in the hybrid aerogel are beneficial for the synergistically enhanced thermal-assisted photodegradation toward VOC-contaminated water with a water evaporation rate of $2.08 \text{ kg m}^{-2} \text{ h}^{-1}$ and a phenol removal efficiency of 94.8%. Our findings may help the development of novel functional nanostructures for applications in environmental remediation and solar steam generation.

1. Introduction

Fresh water shortage crisis has become increasingly serious with the improvement of human living standard, climate change, population growth and industrial development [1,2]. Hence, efficient utilization of abundant seawater and industrial wastewater to produce clean water is one of the most effective strategies to resolve water shortage crisis [3–5]. Up to now, a number of feasible techniques have been employed for high-efficiency wastewater treatment such as semiconductor-based photocatalysis [6–8], solar-driven water evaporation [9–11] and et al. Particularly, solar-powered water evaporation technology could realize environmentally friendly, low-cost and no extra power input clean water production, showing great potencies in sustainable water treatment, which has become a focus and front study filed to resolve the water shortage crisis [12,13].

In such technology, photothermal conversion materials with designed chemistry and structures are the key component to achieve excellent solar evaporation efficiency. In the last few years, various types of photothermal materials including carbon materials [14], plasmonic metal nanoparticles [15], semiconductor particles [16] and polymeric materials [17] have been developed to enhance the water

evaporation efficiency. Furthermore, several strategies have been adopted to improve the water evaporation efficiency such as the enhancement of light absorption to optimize photothermal conversion efficiency [18,19], anti-salt ability [20], regulation of enthalpy of water evaporation [21]. Although these strategies could fulfill the enhancement of water evaporation and high energy efficiency, however, high quality clean water can be only obtained from water sources contained inorganics or most high-boiling point organics. Generally, the source water contains not only salts or high-boiling point organics, but also volatile organic compounds (VOCs) such as phenols [22]. Salts, heavy metal ions and high-boiling point organics will be concentrated in water in evaporation, but VOCs will be easily evaporated along with water and enriched in the distillate water during evaporation [23,24]. Therefore, the treatment of VOC-contaminated water environment is a deadly problem in solar-driven water purification, but to our knowledge, the current research progress about VOC-involved water evaporation treatment is limited. Solar-driven photocatalysis could remove the majority of organic pollutants including VOCs in wastewater through active redox reactions [25–27]. However, due to the limitations of this strategy, many inorganic salts and small molecules will residue in purified water [28,29]. Therefore, it is highly desired to develop novel materials

* Corresponding authors.

E-mail addresses: songhaojie@sust.edu.cn (H. Song), yongli@sust.edu.cn (Y. Li), xiaofei.yang@njfu.edu.cn (X. Yang).

<https://doi.org/10.1016/j.apcatb.2021.120820>

Received 6 August 2021; Received in revised form 8 October 2021; Accepted 11 October 2021

Available online 13 October 2021

0926-3373/© 2021 Elsevier B.V. All rights reserved.

with both high-efficiency water evaporation and superior photocatalytic performance for sustainable water treatment.

As a π -conjugated conducting polymer, polypyrrole (PPy) possesses the merits of outstanding conductivity, environmental stability, superior photo-physical property and excellent carrier mobility [30]. Moreover, recent studies about PPy have been explored for solar-powered energy conversion including photocatalysis and photothermal water evaporation due to its full-spectrum light absorption [31,32]. To achieve the functional synergy between photocatalysis and photothermal effect, two critical factors should be taken into consideration for the material design: (1) abundant pore structure that offers sufficient water transport channels to enable a high solar steam generation rate; (2) efficient charge carrier separation in the illuminated materials to realize superior photocatalytic capacity. Notably, PPy is an agglomerated powder with low charge separation efficiency, which is unable to satisfy the above requirements [33]. Hence, assembling bulk PPy into compact porous aerogels by integrating with carbon-based nanostructures is highly anticipated. As a typical carbon material, graphene aerogels with outstanding light absorption, excellent photothermal conversion, inherent porous structure, higher surface utilization, leads to a myriad of promising applications in solar-driven water purification [34–36]. However, graphene sheets will be liable to restack to form irreversible aggregates due to the π - π conjugation, which limits the accessibility of solid-liquid contact area during the progress of treatment [37]. When PPy assembles into macroscopic hybrid architecture via integrating with graphene aerogels, the Py monomer will be easily anchored on the surface of graphene to be polymerized. In this progress, the self-stacked effect of graphene will be restrained and simultaneously assembles to a 3D loose porous structure, which endows aerogels with large specific surface area for pollutant adsorption, low density for self-floating and abundant pores for water transport and mass transfer in photodegradation and photothermal water purification. And as main photocatalytic active agent, the π - π stacking between PPy and graphene provide more profitable transmission channels for photogenerated electrons generated in PPy, which helps regulate the band structure to produce more active species and restrain the electron-hole recombination [38,39]. The intramolecular coupling favors the formation of π electronic delocalization system and facilitates strong interactions with organic molecules, especially conjugated or nonpolar molecules for the accelerated water evaporation [40].

Herein, we fabricated a holey reduced graphene oxide/polypyrrole (denoted as GR/PPy) aerogel by a facile, eco-friendly method. PPy nanolayers were in-situ grown on the surface of reduced graphene oxide sheets during the formation of aerogels, thereby restraining the self-stacking of 2D nanosheets. The loose and porous structure of GR/PPy aerogels could enhance the light-harvesting property and gas-liquid contact area to provide beneficial open channels for water transport and permeability, leading to a superior solar steam generation performance. PPy nanolayers anchored on reduced graphene oxide nanosheets not only enhance the mechanical strength of aerogels, it also facilitates the migration of photogenerated electrons onto reduced graphene oxide to avoid recombination of charge carriers. Benefit from the rational design, the optimized sample GR/PPy-30 showed excellent solar-driven water purification capacity where the water evaporation rate was $2.08 \text{ kg m}^{-2} \text{ h}^{-1}$ with an energy conversion efficiency of 86.3% under 1.0 sun. Meanwhile, it showed remarkably enhanced photodegradation performance toward different organic pollutants such as MO, RhB, CIP and phenol, implying the potential for simultaneous solar steam generation and organic pollutants removal. More importantly, the hybrid aerogel GR/PPy-30 effectively prevented the accumulation of VOCs in distilled water such as phenol and exhibited a high-efficiency removal of 94.8%. The findings clearly indicate that as-prepared GR/PPy aerogel is a promising material for applying in high-performance and sustainable solar-driven freshwater production.

2. Experimental section

2.1. Materials

All chemicals were purchased from commercial sources and used without further treatment. Graphite, ethyl alcohol ($\geq 99.7\%$) and hydrogen peroxide (30 wt%) were purchased from Sinopharm Chemical Reagent Co. Ltd. Pyrrole (Py, 98%) was from Meryer Chemical Technology Co. Ltd.

2.2. Sample preparation

Graphene oxide (GO) was obtained through a modified Hummers' method as the literature reported [41]. The GR/PPy aerogels were prepared via a one-step and eco-friendly hydrothermal reduction method. Typically, Py (30 μL) monomer and H_2O_2 (0.3 wt%, 5 mL) were mixed with GO dispersion (3 mg L^{-1} , 70 mL), and the mixture was sealed in a 100 mL Teflon reactor. After heating at 180°C for 6 h, the GR/PPy hydrogels were obtained. The obtained hydrogels were purified with ethyl alcohol and deionized water to remove unreacted reagents. Then, GR/PPy aerogels were obtained by freeze-drying. Depending on the Py content (0, 20, 30, 40 and 50 μL), the aerogels were labeled as GA, GR/PPy-20, GR/PPy-30, GR/PPy-40 and GR/PPy-50, respectively.

2.3. Characterization

XRD patterns were obtained on a Bruker D8 Advance X ray diffractometer with $\text{Cu K}\alpha$ radiation source. Infrared spectra (FI-IR) was obtained using Fourier infrared spectrometer (Nicolet, iS 10). The microstructure of aerogel was characterized by field emission scanning electron microscope (HITACHI, SU8100) equipped with X-ray energy dispersive spectroscopy (EDS) for elemental mapping and spherical aberration correction transmission electron microscope (JEOL, ARM300F). Raman spectra was characterized by microconfocal laser Raman spectrometer (Renishaw-invia). The chemical state and molecular structure was carried by X-ray photoelectron spectrometer (XPS) with $\text{Al K}\alpha$ X-ray source (Kratos, AXIS SUPRA). Optical absorbing property was acquired by ultraviolet and visible spectrophotometer (UV-Vis, Agilent, Cary 5000). Fluorescence spectra and Photoluminescence were characterized by fluorescence spectrophotometer (Edinburgh, FS5).

2.4. Solar steam generation test

Solar steam generation test was carried using a solar simulator (Xe lamp, CEL-S500) with an AM 1.5 filter (1.0 sun irradiation, 1000 W m^{-2}). In detail, distilled water (30 mL) was added into a borosilicate glass beaker, and then aerogels were fixed in polystyrene foam to keep floating. Besides, the surface of steam generation system was covered by commercial degreasing cotton to reduce heat loss to the environment. Adjusting the light spot size to ensure consistency with the size of aerogels. The weight loss of water was recorded by recording the weight of samples by the balance every 5 min. The surface temperature of the photothermal aerogel was recorded by an infrared (IR) camera.

2.5. Photocatalytic performance test

The photocatalytic performances of different samples were evaluated under simulated solar irradiation (200–2500 nm, light intensity 100 mW cm^{-2}) by using Rhodamine B (RhB), methyl orange (MO), volatile organic compound (VOC) Phenol and antibiotic ciprofloxacin (CIP) as models. The photocatalytic test was conducted in a double quartz glass beaker with 25°C circulating cooling water. The details are as follows: aerogels were mixed with pollutant solutions (100 mL, 10 mg L^{-1}), and then placed the above mixtures in dark for 60 min to reach adsorption-desorption equilibrium prior to light exposure. Subsequently, the solar

simulator was turned on for photocatalytic degradation and 1 mL solution was taken out to measure its concentration on UV-vis spectrophotometer every 10 min. The remaining of contaminant was expressed as C/C_0 , where C and C_0 represent real-time concentration and initial concentration, respectively.

2.6. Clean distillate water production

Water purification performance of aerogel was evaluated by lab-made evaporation device, and phenol were chosen as model pollutants. The evaporation device was an oil-lamp-like setup by using superhydrophilic commercial degreasing cotton with low thermal conductivity ($\sim 0.04 \text{ W m}^{-1} \text{ K}^{-1}$) to isolate heat transfer between evaporation system and liquid surface. Subsequently, phenol solution (50 mL, 20 mg L^{-1}) was added to the above evaporation device and then the evaporation device was placed in darkness for 1 h to reach adsorption-desorption equilibrium prior to illumination. The phenol concentration in distillate water was characterized by a UV-vis spectrophotometer after 1 h distillation. Furthermore, to simulate the complex water purification process in the real environment, polluted water with complex composition (50 mL) mixed with MO (20 mg L^{-1}), RhB (20 mg L^{-1}), CIP (20 mg L^{-1}) and phenol (20 mg L^{-1}) was used as purified water source.

3. Results and discussion

3.1. Structure and morphology of GR/PPy aerogels

Porous GR/PPy aerogels were synthesized via a one-step hydrothermal method as illustrated in Fig. 1a, in this process, GO was employed as an initiator, H_2O_2 was used as a pore-forming agent and an oxidizing agent. Py monomer was uniformly polymerized on the surface of GO to assemble into nanolayer through the oxidizing action of H_2O_2 and oxygen-containing functional groups in GO [42]. Meanwhile, the defective active sites in GO will be oxidized by H_2O_2 , and leaving nanopores on GO sheets [43,44]. Furthermore, the as-synthesized PPy possesses abundant π - π conjugated structure which could easily link it upon the surface of GO. As well known, RGO sheets with abundant π - π interactions and van der Waals force will induce the reaggregation of RGO sheets leads to low surface area and poor charge transfer performance. The introduction of PPy can anchor on the surface of RGO sheets uniformly and effectively prevent the aggregation of nanosheets, thus forming 3D self-supporting porous structure. As shown in Fig. 1b and c, GR/PPy aerogels exhibited a loose and porous structure compared with pure RGO (Fig. S1). Furthermore, RGO sheets were uniformly covered by PPy nanolayers (Fig. 1d), indicating the effective polymerization of

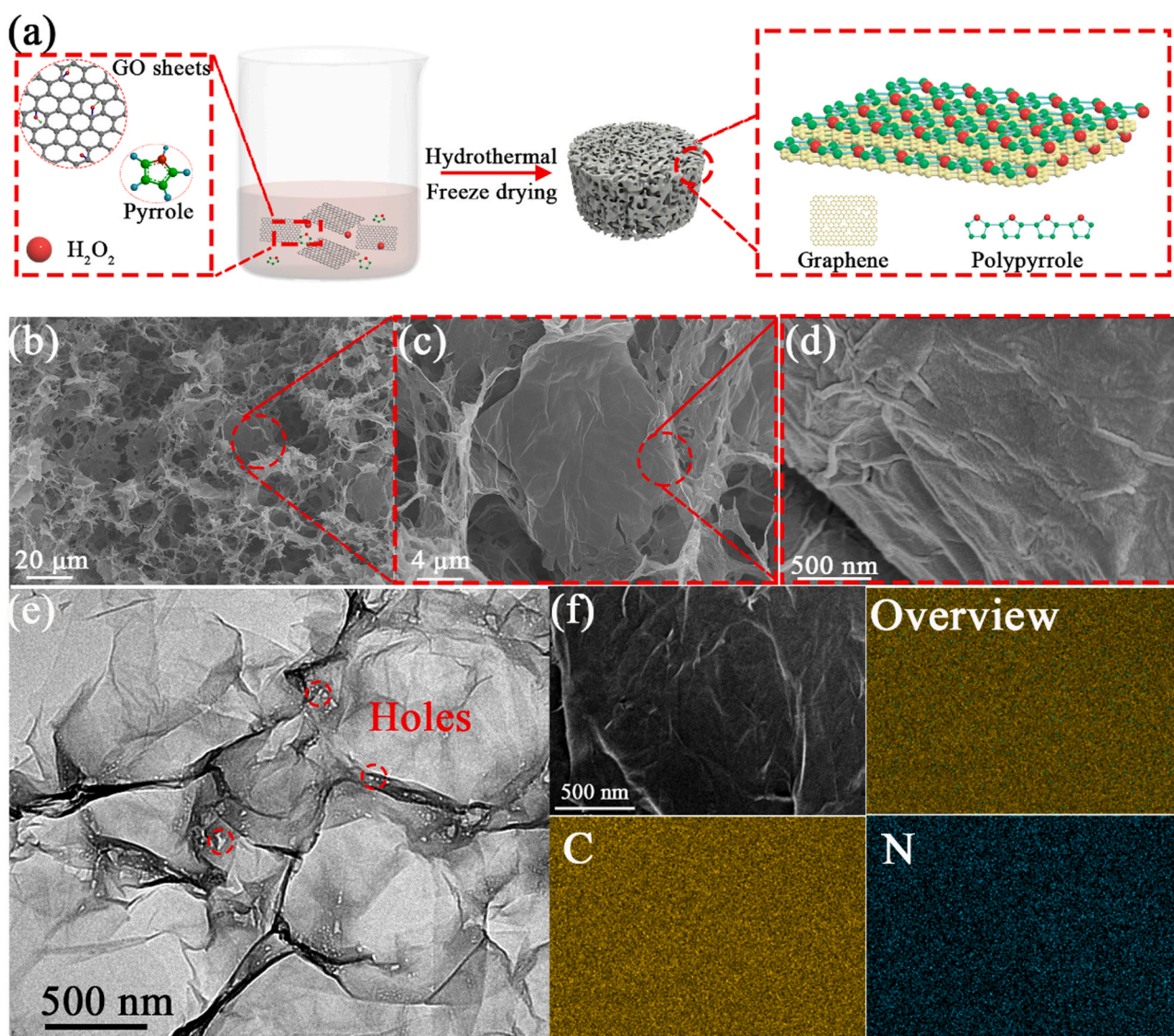


Fig. 1. (a) Schematic illustration of the synthetic process of GR/PPy aerogels. (b–d) SEM images of the GR/PPy aerogel under different magnification. (e) TEM image of the GR/PPy aerogel. (f) EDX elemental mapping analysis of the GR/PPy aerogel.

Py monomer along RGO sheets. Besides, this results are further verified by TEM and EDS (Fig. 1e and f). In Fig. 1e, it can be observed that many nanoholes with diameter about 5–50 nm distributed in RGO sheets, and RGO sheets were covered by PPy nanolayers. The holey RGO with large surface and abundant active sites could promote the rapid transfer of charge by providing more electron transfer junctions [45]. However, original RGO sheets were smooth and intact (Fig. S2). In addition, the N elements in PPy exhibit a uniform distribution, indicating the introduction of PPy nanolayers (Fig. 1f). Therefore, the porous structure of GR/PPy aerogels could not enhance the water transport but also be beneficial to the light harvesting property and pollutants adsorption. Meanwhile, uniform PPy nanolayers on the RGO surface makes the pollutants contact with active sites more easily. This unique structure would be conducive to enhance the water evaporation and photocatalytic performance of GR/PPy aerogels.

As shown in Fig. 2, various methods including FT-IR, XRD, Raman spectroscopy, and XPS were utilized to investigate the interaction and chemical states of GR/PPy aerogels. In Fig. 2a, for the FT-IR spectra of GO, the dominant absorption peaks at 1735 cm^{-1} , 1622 cm^{-1} , 1385 cm^{-1} , 1224 cm^{-1} , and 1053 cm^{-1} represent carbonyl C=O, C=C, O=C-O stretching vibrations, C-O-C, C-O stretching vibrations of the oxygen functional groups, respectively. However, the oxygen-containing groups C=O, C-O-C and C-O in GA and GR/PPy almost vanished after hydrothermal treatment, indicating the most the oxygen-containing groups were removed sufficiently. In GR/PPy, the characteristic band in 1622 cm^{-1} moved to 1549 cm^{-1} , this band corresponds to the typical PPy asymmetric and symmetric ring vibration of C-H, illustrating obvious π - π conjugation effect exists in GR/PPy. And the bands located at 1177 and 973 cm^{-1} were for $=\text{N}^+$ bipolaron vibration

of PPy, 1035 cm^{-1} is related to $-\text{N}^+$ polaron in plane vibration [46]. The final, the band attribute to C-H out of plane vibration was observed at 797 cm^{-1} . Hence, the π - π conjugation effect between RGO and PPy can produce more delocalized electrons while reducing the transition barrier of electrons to make the migration of electrons more easily [47–49]. It is remarkable that FT-IR demonstrated the presence of polarons and bipolarons, which can effectively promote electron migration due to their capture and release of electrons. In Fig. 2b, XRD patterns of GO exhibits a sharp and strong diffraction peak at 10° , which corresponds to the (001) diffraction. While for GA and GR/PPy, the diffraction peak of GO at about 10° disappeared, and a wide diffraction peak appears about $2\theta = 25^\circ$, which corresponds to (200) crystal planes, indicating the effective reduction of GO. It is worth noting that the diffraction peak in GR/PPy shifted from 24.5° to 25° compared with that in GA, indicating the efficiently coupling between RGO sheets and PPy nanolayers [50]. To further unveil the structural characteristics of GO, GA and GR/PPy, Raman spectroscopy was adopted to verify. As shown in Fig. 2c, GO and GA show two distinct peaks in 1340 cm^{-1} and 1588 cm^{-1} , which are associated with the D and G bands, relating to sp^3 hybridized carbon atoms and the vibration of sp^2 carbon atoms, respectively. The ratio of D to G band intensity is generally used to indicate crystallinity of GO. The I_D/I_G values of GO and GA increased from 0.87 (GO) to 1.02 (GA), indicating the size of sp^2 domains increased [51]. Due to the D and G band of PPy is located at 1567 and 1341 cm^{-1} , the above bands of GR/PPy are shifted to 1343 and 1572 cm^{-1} , which reveals the π - π conjugation interaction between PPy and RGO sheets [52]. Moreover, the I_D/I_G of GR/PPy values reached 1.10, implying there are abundant active defects. XPS spectra of GO, GA and GR/PPy was testified to clarify their chemical bonding state, which was shown in Fig. 2d–i. For GO and

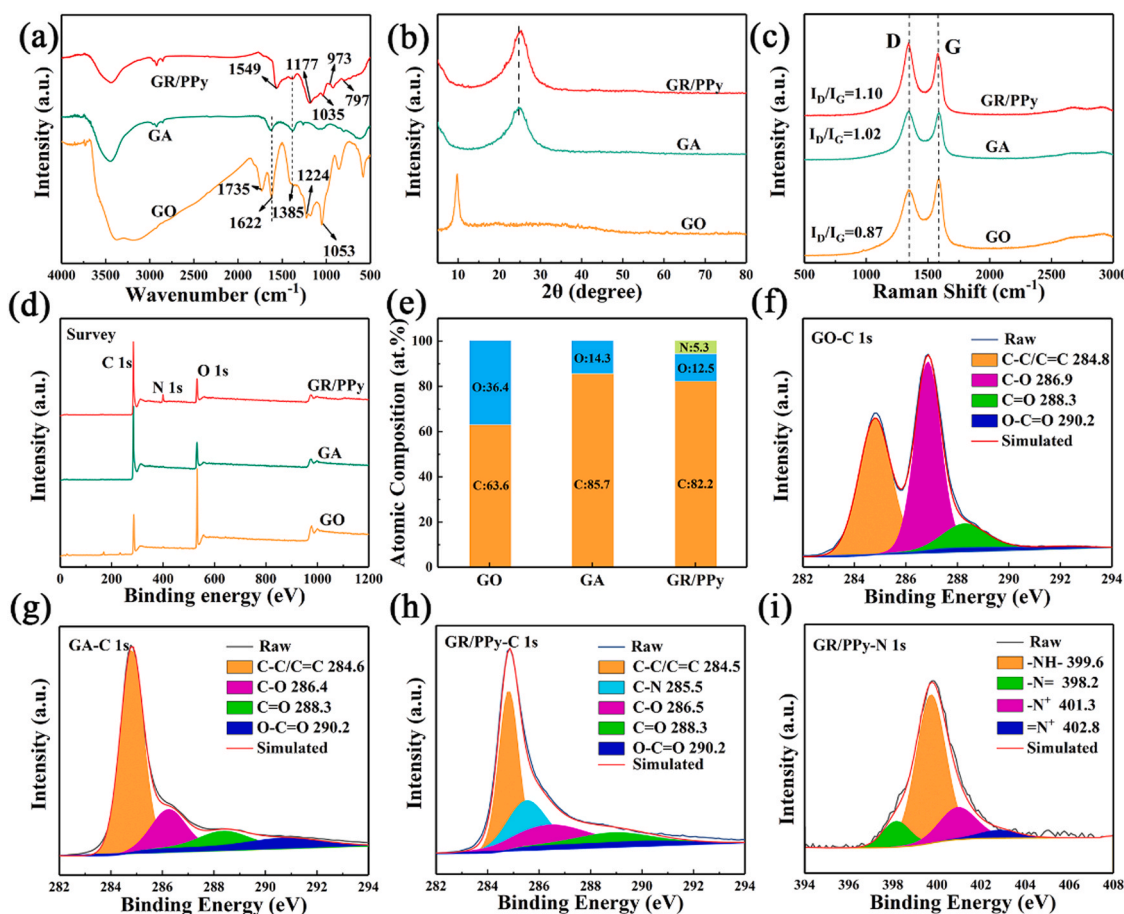


Fig. 2. (a) FT-IR spectra; (b) XRD patterns; (c) Raman spectra; (d) XPS survey spectra of GR/PPy. (e) The atomic percentages of C, O, and N in GO, GA and GR/PPy. XPS C 1s of (f) GO; (g) GA; (h) GR/PPy. (i) N 1s of GR/PPy.

GA, it was shown that only the characteristic peaks of C 1s and O 1s in can be detected, however, in GR/PPy aerogel, additional characteristic peaks of N 1s in 398 eV can be observed because of the existence of PPy (Fig. 2d). According to the ratio of atomic composition, the content of oxygen atom on RGO nanosheets decreased obviously after thermal reduction, indicating that most GO sheets were reduced to RGO (Fig. 2e). In addition, residual oxygen illustrates the presence of dangling bonds in holes on RGO sheets which is caused by the oxidation of H_2O_2 .

Meanwhile, high-resolution spectra of C 1s of GO, GA and GR/PPy further indicate that the oxygen functional groups in GO such as C-O (~ 286 eV), C=O (~ 288 eV) have been removed via thermal reduction (Fig. 2f–h). Besides, in GR/PPy, additional C–N bond was observed at the binding energy of 285.5 eV, suggesting that the incorporation of PPy in graphene. The N 1s spectra of GR/PPy can be decomposed into four components (Fig. 2i), at binding energies of 398.2, 399.6, 401.3 and 402.8 eV, the peaks correspond to $-\text{N} =$, $-\text{NH}-$, $-\text{N}^+$ and $=\text{N}^+$, respectively. The $-\text{N}^+$ and $=\text{N}^+$ represent polaron and bipolaron respectively, namely positively charged nitrogen species of oxidized amine and protonated imine [53–55]. In addition, the obvious peaks of positively charged nitrogen declares the PPy possesses a certain doping level, and the polaron and bipolaron in PPy can effectively promote electron migration due to their capture and release of electrons [56,57].

The properties of the synthesized GR/PPy aerogels can be controlled by adjusting the amount of Py. Fig. 3a displayed the effect of Py content on the appearance of aerogels, which shows that with the content increasing, the volume of GR/PPy increased. This result indicated that Py consumes H_2O_2 , resulting in RGO sheets not be etched into porous structure, meanwhile, the polymerized PPy makes RGO sheets form three-dimensional structures. The SEM of GR/PPy aerogels with different also confirms the conclusion. As shown in Fig. 3b–f, for GA, RGO sheets were over-etched by excessive H_2O_2 , resulting in almost no intact flakes exist. In addition, the lack of PPy caused more self-stacked behavior of RGO sheets via π - π conjugation interaction, thus making the structure more compact. With the increase of Py content, the fewer holes etched on RGO, the more intact nanosheets exist due to the competitive effect of Py on H_2O_2 . Moreover, when added a high content of Py, the polymerized PPy can effectively prevent the self-stacking of RGO sheets, so the aerogel shows a thinner three-dimensional lamellar stacking structure, thereby showing a larger shape. It is worth noting that the aerogel is larger when Py is added without H_2O_2 (Fig. S3), which is because Py is only attached to RGO sheets by physical adsorption to enlarge the interlayer spacing and intact nanosheets accumulate a larger three-dimensional structure. Therefore, based on this phenomenon, the

properties of the synthesized GR/PPy aerogels can be controlled by adjusting the amount of Py.

Fig. 4 shows the physical properties of the prepared GR/PPy aerogels with different Py content. The specific surface area and pore size distributions of GR/PPy aerogels were characterized by N_2 adsorption-desorption measurements. As shown in Fig. 4a, the N_2 adsorption-desorption curves show typical type-I isotherm models. The surface areas of different GR/PPy aerogels are estimated to be 146.7, 154.3, 269.4, 256.4 and $166.9 \text{ m}^2 \text{ g}^{-1}$, respectively. Besides, the pore-size distribution curve shows that the pore size of all GR/PPy aerogels is about 10–20 nm (Fig. 4b). These results indicate the as-synthesized aerogel can effectively transport water and adsorb pollutants due to its large specific surface area and rich pore structure. Fig. 4c shows that the density of GR/PPy aerogels is greatly influenced by Py content. Without Py, due to the self-stacking effect of GO sheets, GO sheets will agglomerate which caused the formed GA aerogel exhibited dense structure and large density. However, with the increase of Py, the density of aerogels decreased significantly, this phenomenon comes from the fact that PPy could be anchored onto the surface of RGO sheets through π - π interaction, which will restrain the self-stacking of nanosheets thereby forming larger and more fluffy aerogels [58,59]. Besides, different Py additions make the density of aerogels different, and the density is minimum in GR/PPy-30, which is 9.6 mg cm^{-3} and can be easily supported by a leaf, reaching the standard of ultralight materials (density $< 10 \text{ mg cm}^{-3}$). Nevertheless, with less Py content (GR/PPy-20), some RGO sheets will occur self-stacking phenomenon due to the lack of PPy, so its density is larger than GR/PPy-30. On the contrary, in GR/PPy-40 and GR/PPy-50 with high Py content, due to the excessive consumption of H_2O_2 in the pyrrole polymerization process, resulting in a decrease in the number of pores on RGO sheets and the increase of the density of GR/PPy aerogels. Besides, this result is consistent with the SEM analysis, indicating that the content of Py will restrain self-stacked behavior and porosity of RGO nanosheets in GR/PPy aerogels. Notably, the preparation of ultralight carbon-based aerogels (density $< 10 \text{ mg cm}^{-3}$) usually requires high temperature treatment, otherwise the density of obtained aerogel is usually high [60]. However, in Fig. 4d, compared with other aerogels reported in literatures, GR/PPy-30 can obtain lower density at lower synthesis temperature (180°C). Furthermore, in Fig. 4e, the as-prepared GR/PPy-30 has superior mechanical strength and can support about 1000 times of its own weight without deformation. The stress-strain curve shows under 17% strain, the compressive stress of GR/PPy-30 reaches peak value about 13.1 kPa. Furthermore, compared with the average modulus of other reported carbon-based aerogels (Fig. 4f), GR/PPy-30 shows superior mechanical strength, indicating it possesses

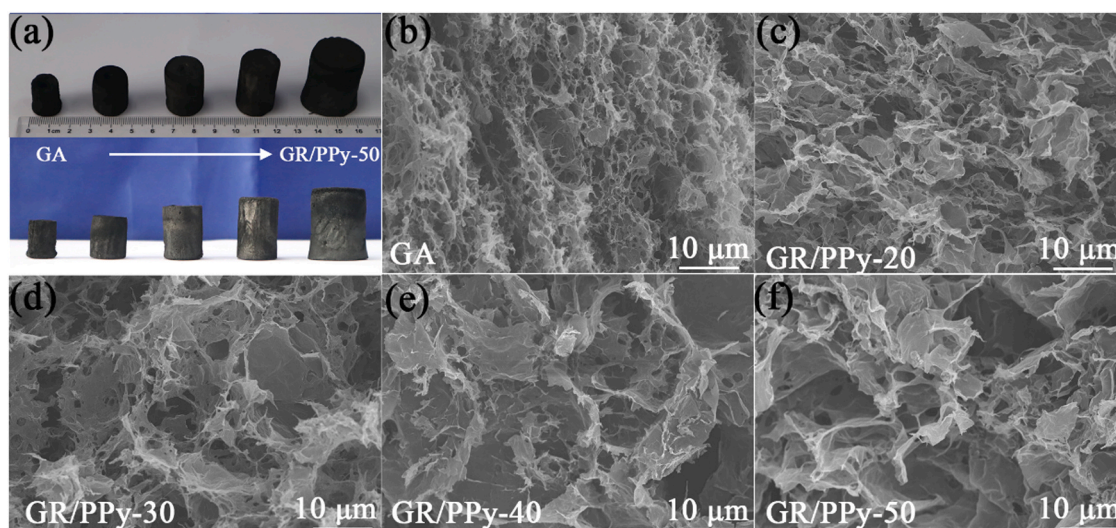


Fig. 3. (a) Photographs of different GR/PPy aerogels. SEM images of GA (b), GR/PPy-20 (c), GR/PPy-30 (d), GR/PPy-40 (e), GR/PPy-50 (f), respectively.

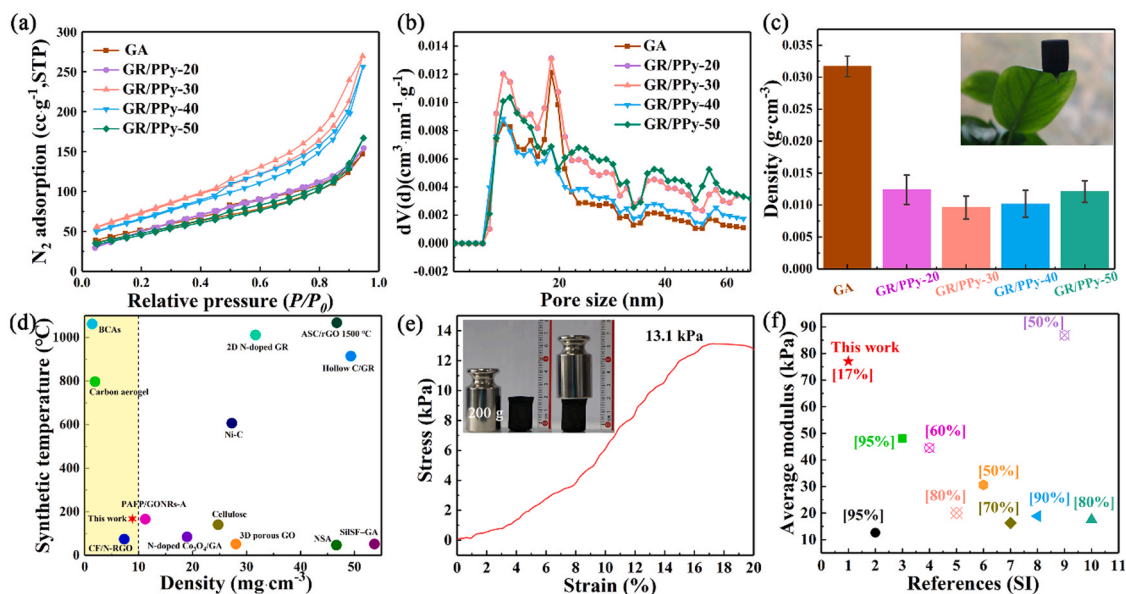


Fig. 4. (a) N_2 adsorption-desorption isotherms of different GR/PPy aerogels. (b) Pore size distribution for GR/PPy aerogels obtained via the non-localized density functional theory (NLDT) model. (c) Density of different GR/PPy aerogels. (d) Comparison of density and synthetic temperature of different aerogels, and the yellow area is ultralight materials (density $< 10 \text{ mg cm}^{-3}$, Refs. [6–26] in Supporting Information). (e) Stress-strain curve of GR/PPy-30 aerogel with 20% maximum strain. (f) Comparison of the average modulus with different carbon-based aerogel, Refs. [19–27] in Supporting Information, [17%] represents maximum strain of GR/PPy-30 aerogel.

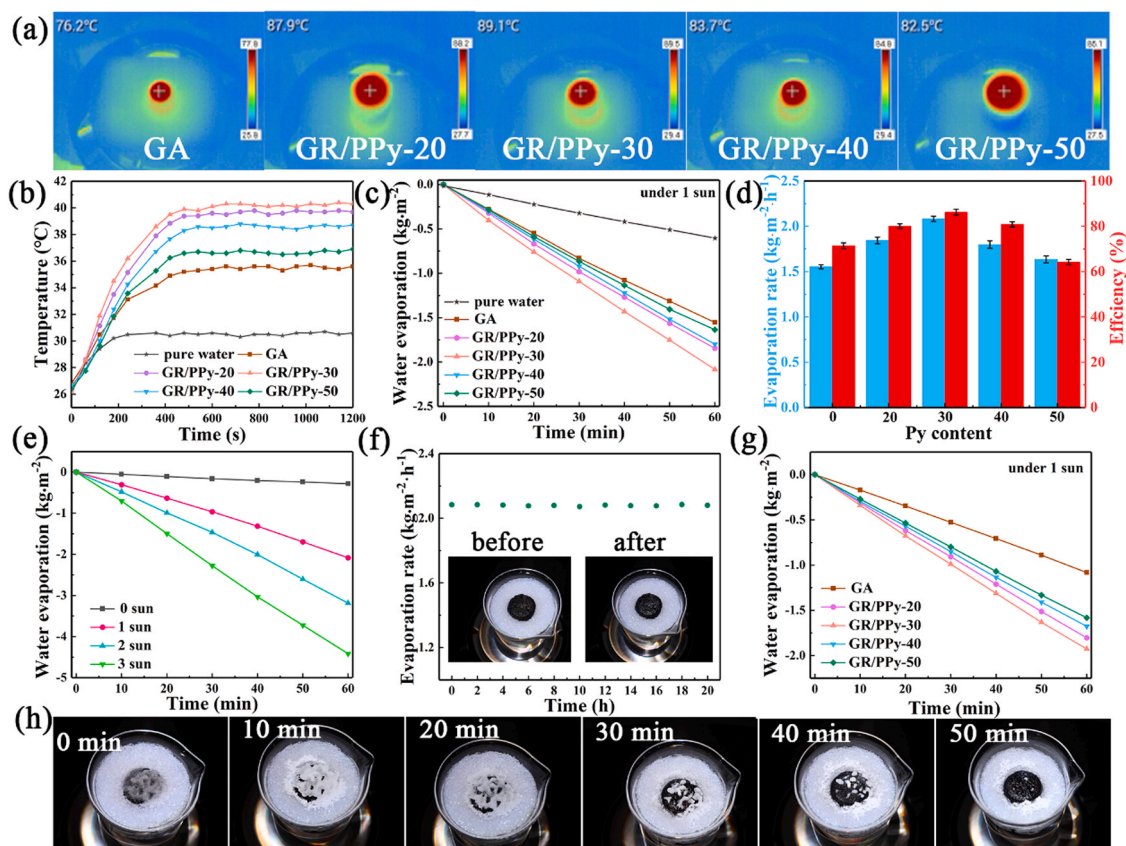


Fig. 5. (a) IR images of different GR/PPy aerogels in air under 1 sun irradiation. (b) Temperature change with time of different GR/PPy aerogels in water. (c) Water evaporation amount of different evaporators under 1.0 sun irradiation. (d) Evaporation rate and energy conversion efficiency of different evaporators. (e) Water evaporation amount of GR/PPy-30 evaporator under 0, 1, 2 and 3 sun irradiation, respectively. (f) Cycling stability of GR/PPy-30 evaporator. (g) The evaporation rate of GA and different GR/PPy aerogels in 15 wt% NaCl solution under 1 sun irradiation. (h) Typical optical images of the salt accumulation and dissolution on the GR/PPy-30 evaporator.

excellent mechanical stability for as a structural material. In conclusion, due to the self-stacked behavior of graphene is restrained by PPy, which contributes to increase the usable graphene sheets amount to enhance the stability of aerogel and increase the amount of loose and porous structure. Therefore, this phenomenon endows GR/PPy-30 excellent mechanical strength and abundant porous structure for solar-driven water purification.

Besides, the superwetting behavior of aerogels was tested via a high-speed video camera (Fig. S4). The result shows that as the PPy content increases from 0 to 50, the surface of aerogels becomes more and more hydrophobic. GA aerogel can be fully wetted less than 0.1s, this result indicates the residual oxygen-containing functional groups on the graphene sheets efficiently enhanced the contact of aerogels with aqueous solution to increase the water transport [61]. With the increase of PPy content, the competition between PPy and H_2O_2 leads to the reduction of nanopores on RGO sheet, thereby decreasing the internal oxygen-containing functional groups. Hence, the time for RGO to be fully wetted is gradually increased. The result showed that on the surface of GR/PPy-40 and GR/PPy-50, the water droplet shows a regular half sphere shape and then retained relatively long time (more than 2 s), which illustrates high content PPy has an adverse effect on wettability of aerogels.

3.2. Photothermal evaporation properties of GR/PPy aerogels

The superior light absorption properties in the wavelength range of sunlight for as-prepared GR/PPy aerogels were shown in Fig. S5. In Fig. S5a, due to the superior absorption over the whole solar spectrum of PPy, the light absorption capacity of GR/PPy aerogels is obviously higher than that of GA aerogel. And GR/PPy-30 possesses strongest light absorption among them. Meanwhile, GR/PPy-30 shows highest solar absorption intensity (Fig. S5b). The phenomenon illustrates that PPy can effectively improve the light absorption properties of GR/PPy aerogels, thereby improving their light-to-thermal conversion effect and photocatalytic performance. In Fig. 5a, the steady-state temperature in air under 1.0 sun irradiation of different GR/PPy aerogels GA, GR/PPy-20, GR/PPy-30, GR/PPy-40 and GR/PPy-50 are 76.2, 87.9, 89.1, 83.7 and 82.5 °C, respectively, and this result is consistent with the light absorption capacity of GR/PPy aerogels, which indicates that the addition of PPy could efficiently enhance the light-to-thermal conversion effect of aerogels. Based on this, the advantages of GR/PPy aerogels including unique porous structure, superior optical properties and light-to-thermal conversion efficiency make it have potential as an advanced photothermal evaporation material. The performance of GR/PPy aerogels for solar-steam generation was evaluated using a device in Fig. S6. The surface temperature changes of photothermal GR/PPy aerogels were measured by IR image system. In Fig. 5b, under 1.0 sun irradiation, the surface temperature in water of aerogels first increased and then kept at a stable value. Since GR/PPy-30 has high light absorption capacity, it exhibits the maximum heating rate and equilibrium temperature, and the surface temperature rises from 26.2 °C to 33.8 °C in 500 s, then stay stable about 40.3 °C in 1200 s, followed by GR/PPy-20, GR/PPy-40, GR/PPy-50, GR/PPy-0 and pure water. Obviously, compared with pure water and GR/PPy-0, GR/PPy-30 has excellent photothermal conversion ability, which can effectively improve the water temperature to drive water evaporation. The water evaporation performance of the aerogels was investigated by measuring the mass of the evaporated water under 1.0 sun irradiation and shown in Fig. 5c. It was observed that a low water evaporation amount (0.48 kg m^{-2}) was obtained in pure water. However, in the presence of GR/PPy aerogels the water evaporation amount exhibited dramatic weight loss under the same experimental conditions. The obtained water evaporation amounts under 1.0 sun irradiation of GA, GR/PPy-20, GR/PPy-30, GR/PPy-40 and GR/PPy-50 were 1.55, 1.84, 2.08, 1.80 and 1.63 kg m^{-2} , respectively. The corresponding evaporation rate are 1.55, 1.84, 2.08, 1.80 and $1.63 \text{ kg m}^{-2} \text{ h}^{-1}$ (Fig. 5d). Consequently, the energy conversion

efficiency of different GR/PPy aerogels are 71.4%, 80.1%, 86.3%, 80.85% and 64.2%, respectively. In GA without PPy, the self-stacked effect of graphene sheets will occur in the formation of graphene aerogels, which adversely affects the internal pore structure of graphene aerogels and reduces the transport of water. Hence, in this case, GA shows a relatively low evaporation rate $\sim 1.55 \text{ kg m}^{-2} \text{ h}^{-1}$ compared to GR/PPy aerogels. However, the evaporation performance improvement of GR/PPy benefited from the synergistic effect of GR and PPy. Firstly, as a π - π conjugated polymer material, its broadband optical absorption and excellent energy efficiency can absorb the full spectrum solar energy and convert it to thermal efficiently via its molecule thermal vibration effect. In this case, PPy acts as main light absorber which could effective absorb solar energy and convert to heat for steam production. When it is combined with graphene sheets to form GR/PPy aerogels, the outstanding optical properties of PPy and RGO can increase the light absorption of aerogels, thereby converting more solar energy into heat to generate steam. Moreover, PPy can be absorbed on the surface of RGO nanosheets via π - π interaction which can effectively prevent the self-stacked effect. Hence, the addition of PPy can increase the amount of usable RGO sheets to make GR/PPy aerogels more loose, which could facilitate water transport and the escape of steam to enhance the evaporation performance. But in GR/PPy-20, GR/PPy-30, GR/PPy-40 and GR/PPy-50, GR/PPy-30 exhibited optimal evaporation capacity, which illustrates that the amount of PPy can affect the evaporation capacity. In GR/PPy-20, due to the low content of PPy, the self-stacking effects of RGO sheets in aerogel decrease the amount of internal channel. Besides, due to the low content of PPy, it is difficult to absorb more solar energy to induce photothermal conversion effect, which is consistent with the result of light absorption. However, in GR/PPy-40 and GR/PPy-50, higher PPy content reduces the number of nanopores on RGO nanosheets and hydrophilicity, resulting in a lower water transport efficiency. Therefore, in GR/PPy-30, the superior evaporation performance is mainly determined by the following three aspects: (i) the increase of light absorption capacity via the π - π interaction between RGO and PPy, (ii) an increase of water wettability based on its outstanding hydrophilicity and large specific area, (iii) appropriate porous structure providing more water transport channels.

Fig. 5e shows the plots of the weight loss-time function of the GR/PPy-30 under different illumination intensities. Additionally, in Fig. 5f, the evaporation efficiency of GR/PPy-30 aerogel remains basically unchanged under uninterrupted working for 20 h, which illustrates that it possesses excellent durability. Meanwhile, the evaporation rates of GR/PPy aerogels were evaluated to prove their universality. As shown in Fig. 5g, the obtained water evaporation rates in 15 wt% NaCl solution under 1.0 sun irradiation of GA, GR/PPy-20, GR/PPy-30, GR/PPy-40 and GR/PPy-50 are 1.08, 1.80, 1.93, 1.68 and 1.58 kg m^{-2} , respectively. This results demonstrate that the evaporation rates of different GR/PPy aerogels in NaCl solution are consistent with the trend of pure water, and GR/PPy-30 exhibits the best water evaporation rates. Compared with the evaporation rates of GR/PPy aerogels in pure water, the evaporation rate of aerogels in NaCl solution has no significantly change. However, the evaporation rate of GA was only 1.08, which exhibited a significant decrease compared to the evaporation rate in pure water. This result indicates that the self-stacking effect of RGO sheets could form a denser structure of GA to accelerate the deposition of salt, thereby reducing the evaporation rate of GA. Therefore, PPy will effectively inhibit the self-stacking of RGO nanosheets and makes the GA/PPy aerogels form a fluffy porous structure, which can effectively prevent salt deposition and exhibit excellent salt resistance. Furthermore, the salt resistance of GR/PPy-30 aerogel was carry out by placed 1 g solid NaCl onto the surface of GR/PPy-30 aerogel solar evaporator to proceed continuous evaporation experiments (Fig. 5h). It was noticed that NaCl solid on the surface of GR/PPy-30 aerogel gradually disappeared with the passage of time within 50 min. This phenomenon derives from the fact that aerogel has more porous structures, which can effectively induce salt transport. In summary, GR/PPy-30 aerogel have

excellent photothermal evaporation efficiency and self-desalting effect, which can be effectively used in seawater desalination.

3.3. Photocatalytic property of GR/PPy aerogels

Considering that in most waters contains harmful organic pollutants such as VOCs, dyes, antibiotics and so on, thus only has a single photothermal evaporation cannot satisfy practical requirement. PPy is an emerging organic photocatalyst, which can exhibit significant photocatalytic performance under illumination [62]. Graphene has excellent electron transport properties and large specific surface area, which can effectively promote the separation of photogenerated electrons, thereby enhancing the photocatalytic performance. In addition, both of them have high light absorption. The combination of their light adsorption ability and charge transfer property can improve the light absorption and carrier separation efficiency of the composites, thereby enhancing the photocatalytic performance of the materials. Hence, the photocatalytic properties of GR/PPy-30 under simulated sunlight were investigated. UV-vis absorbance curves of the degradation for organic pollutants at different reaction time using GR/PPy-30 are shown in Fig. 6a–d. It can be seen that the characteristic peaks of organic pollutants rapidly attenuate and finally disappear as the reaction progress, indicating organic pollutants degraded by GR/PPy-30 under simulated solar irradiation. Besides, the temporal evolution of MO concentration in presence of different GR/PPy aerogels was investigated in Fig. 6e. First, the self-degradation of MO under illumination was studied, which indicates that MO was stable under illumination without obvious photolysis. In dark reaction, all aerogels exhibited excellent adsorption

properties (all over 40%) due to their large surface area and porosity, which could absorb abundant organic pollutants and deliver to catalytic active sites, thus contributing to enhanced photocatalytic performance. The photocatalytic degradation experiment of MO shows that GR/PPy-30 possesses the best photocatalytic efficiency, and the degradation rate reaches 95.2% in 60 min under simulated sunlight. The photodegradation efficiencies of GR/PPy-20, GR/PPy-40 and GR/PPy-50 are 85.7%, 88.4% and 91.4%, respectively. For GA, due to the absence of PPy, the aerogel has almost no photocatalytic effect. Therefore, the result indicates that PPy can generate photogenerated carriers under light to conduct redox reaction with pollutants for catalytic degradation. Furthermore, the pseudo-first-order kinetics constant is a convenient index to evaluate the photocatalytic degradation behavior, which could be described as follows: $-\ln \frac{C_t}{C_0} = kt$, where C_t the real-time concentration at t time; C_0 concentration of organic pollutants after dark adsorption; k -apparent kinetic constant; t -irradiation time. According to the pseudo-first-order kinetic curves (Fig. 6f), the obtained k values of GA, GR/PPy-20, GR/PPy-30, GR/PPy-40 and GR/PPy-50 are estimated to be 0.00262, 0.02221, 0.03713, 0.02493 and 0.02938 min^{-1} , respectively. GR/PPy-30 aerogel exhibited a higher photodegradation toward MO in comparison to other aerogels, which is 14 times than that of degradation rate constant of GA. These results suggest that the GR/PPy-30 aerogel is a promising photocatalyst for the degradation of organic pollutants. Meanwhile, the photocatalytic degradation experiments of different samples toward RhB were also carried out. As shown in Fig. 6g, the degradation efficiency of GR/PPy-30 for RhB solution is 96.4%, and the degradation efficiency is still GR/PPy-30 > GR/PPy-50 > GR/PPy-40 > GR/PPy-20 > GA. In

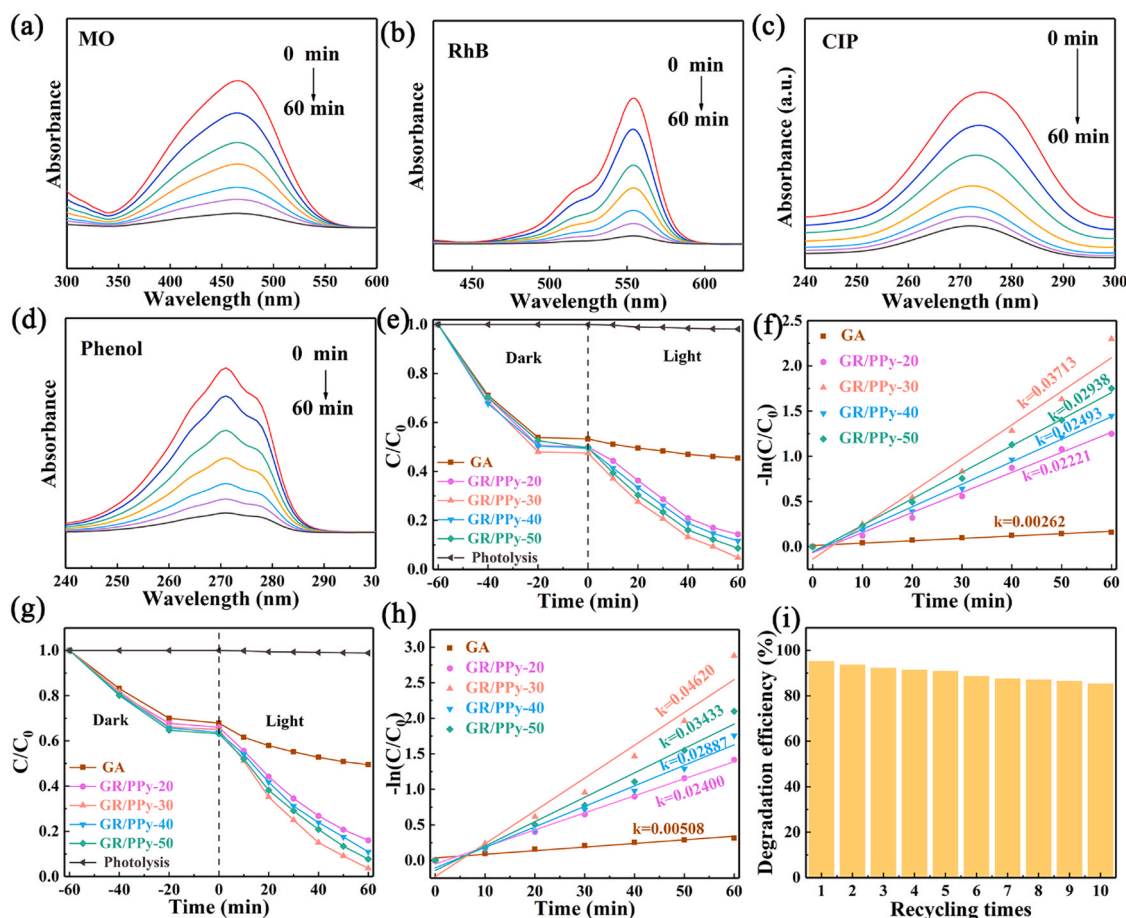


Fig. 6. UV-vis curves at different reaction time of (a) MO, (b) RhB, (c) CIP and (d) phenol on GR/PPy-30 aerogel. Photodegradation curves over different GR/PPy aerogels for (e) MO and (g) RhB. The kinetic curves of GR/PPy aerogels fitted via a pseudo-first-order reaction model, (f) MO, (h) RhB. (i) Recycling ability of GR/PPy-30 aerogel on MO degradation.

addition, the kinetic constants follow this trend (Fig. 6h), indicating that GR/PPy-30 has the best photocatalytic performance. Due to the good loading of PPy on RGO nanosheets, GR/PPy-30 aerogel with large surface area and high porosity can adsorb more pollutants and transfer them to active sites. In addition, as shown in Fig. S7, GR/PPy-30 possesses narrow band gap (1.42 eV) which could make it easier to excite electrons and generate electron-hole pairs under illumination to participate in the catalytic reaction, thereby exhibiting the highest photocatalytic degradation efficiency. GR/PPy-30 also exhibited excellent photocatalysis effect towards phenol and CIP (Fig. S8), the degradation efficiency is respectively 92.5% and 82.6% under 60 min simulated sunlight irradiation with cooling water. Meanwhile, the cyclic degradation tests were used to evaluate the cyclic stability of GR/PPy aerogel, which is shown in Fig. 6i and Fig. S9. The cycle stability of GR/PPy-30 aerogel was tested through 10 cycle simulation experiments. The results show that its degradation efficiency did not decrease significantly compared with the initial degradation efficiency, except for the inevitable loss in the recover process. Therefore, this results verify that GR/PPy-30 possesses excellent stability and recycling performance. Based on the above discussion, GR/PPy-30 was selected for subsequent water purification experiment due to its excellent photocatalytic degradation performance and cycle stability.

In RGO/PPy aerogel photocatalysts, it is proposed that the main factors contributing to different photocatalytic properties of GR/PPy aerogels are the photoelectric effect and charge separation efficiency. In order to investigate the separation efficiency and recombination efficiency of photogenerated carriers, the time-resolved photoluminescence spectroscopy of the GR/PPy aerogels catalysts at 425 nm and electrochemical impedance spectroscopy (EIS) were measured. As shown in Fig. 7a–e, the average lifetimes of photogenerated carriers (τ_1) of GA, GR/PPy-20, GR/PPy-30, GR/PPy-40 and GR/PPy-50 were 0.11, 0.15, 0.24, 0.19 and 0.14 ns, respectively. Generally, a longer carriers average lifetime is related to the slowly recombination rate of the charge carriers [63,64], hence, it can be clearly seen that the τ_1 value of GR/PPy-30 is less than that of other aerogels, which signifies that the photogenerated electron-hole pairs separation was more efficient in GR/PPy-30. This result proves that the photogenerated electrons in PPy HOMO can be rapidly inject in to the surface of RGO due to the quick interfacial charge transfer, which effectively suppresses the recombination of photogenerated carriers to extend the lifetime of photogenerated

electron-hole pairs [65]. Therefore, GR/PPy-30 exhibited the best quantum efficiency, so it has higher photocatalytic efficiency. Furthermore, electrochemical impedance spectroscopy (EIS) results of the aerogels are shown in Fig. 7f, it is obvious that the radius of GR/PPy-30 is the smallest among all the aerogels, indicating GR/PPy-30 possesses the smallest resistance and the fastest photogenerated carriers migration rate.

3.4. Solar-driven purification of complex waste water

To date, one of the critical challenges in the practical application of water purification technology is that most of the wastewater contain many kinds of organic pollutants (soluble, insoluble and volatile organic pollutants), so it is difficult to be treated in one step. Furthermore, as the temperature of the contact surface increases due to the photothermal conversion effect, a large number of VOCs will be transferred to the distillate water with the evaporation process, resulting in the enrichment of pollutants. GR/PPy-30 aerogel has excellent photothermal evaporation capacity and photocatalytic effect, which can effectively purify complex wastewater. Therefore, the freshwater production potential of GR/PPy-30 aerogel was explored by adopting different to water environment was explored. Fig. 8a shows the water evaporation of GR/PPy-30 in different solutions (oil-water emulsion, seawater, deionized water, MO, acid and alkali solution), under 1.0 sun irradiation, the evaporation of oil-water emulsion, seawater, deionized water, MO solution, acid and alkali solution were 1.88, 1.98, 2.08, 2.02, 2.05 and 2.04 kg m⁻², respectively, which is close to the water evaporation in deionized water of 2.08 kg m⁻². From Fig. 8b, it is noted that the calculated evaporation rate of GR/PPy-30 for different solution was 1.88, 1.98, 2.08, 2.02, 2.05 and 2.04 kg m⁻² h⁻¹, respectively. Besides, both the energy conversion efficiency of GR/PPy-30 in the above solution was calculated to be above 80%. This phenomenon illustrates that GR/PPy-30 possesses excellent applicability in different water environment and can be efficiently used to purify complex water environment. In Fig. 8c, the ion concentrations in collected distilled water were obviously lower than that in the salt water which were greatly lessened from the initial concentrations of 14536 (Na⁺), 1450 (Mg²⁺), 1056 (K⁺) and 926 mg L⁻¹ (Ca²⁺) to 12.5 (Na⁺), 0.09 (Mg²⁺), 0.35 (K⁺) and 0.42 mg L⁻¹ (Ca²⁺), respectively. This is equivalent to more than 99.9% ions removed in collected distilled water and the ions

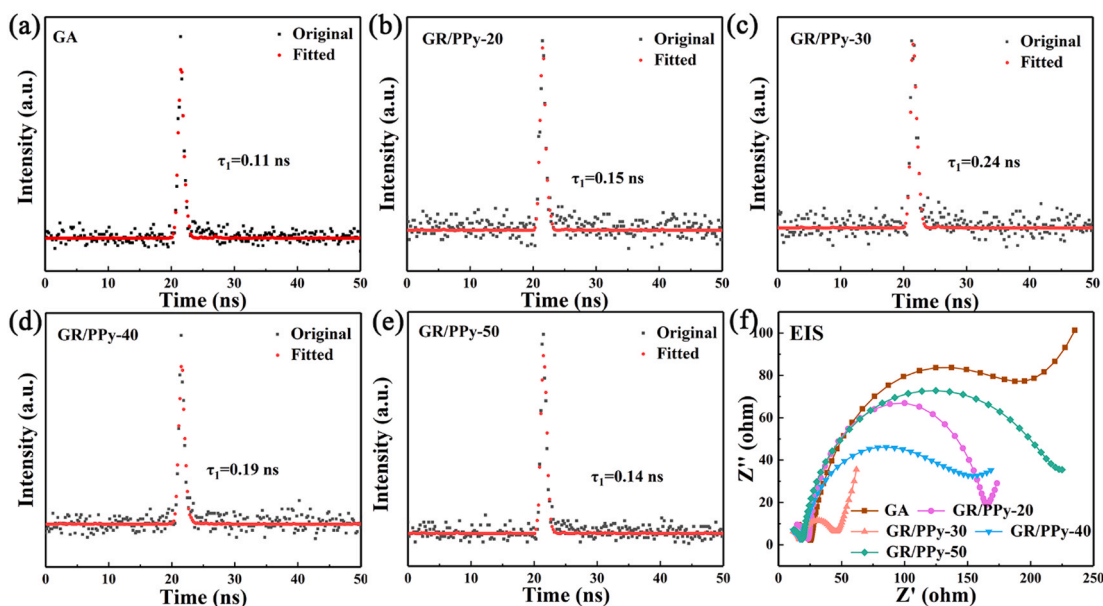


Fig. 7. (a–e) TRPL spectroscopy of different GR-based aerogels. (f) electrochemical impedance spectroscopy of different GR-based aerogels.

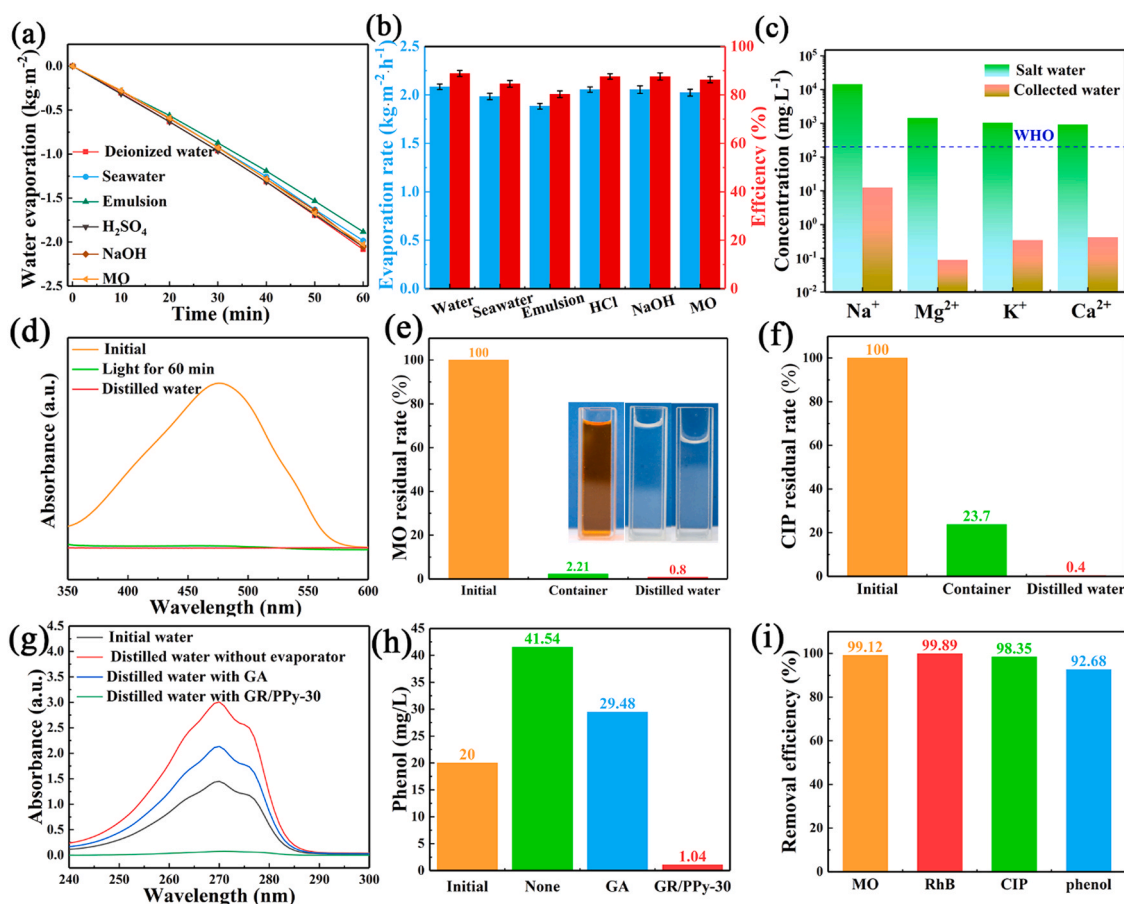


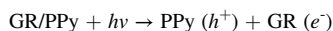
Fig. 8. (a) Water evaporation amount of GR/PPy-30 in different water source under 1.0 sun irradiation. (b) Corresponding evaporation rate and energy conversion efficiency. (c) Comparison of ion concentration in distilled water and synthetic seawater. (d) UV-vis curves of MO in different states on GR/PPy-30. (e) MO residual rate in different states. (f) CIP residual rate in different states. (g) UV-vis curves of phenol on different evaporators. (h) Corresponding concentration of phenol on different evaporators. (i) Removal efficiency of organic pollutants in complex wastewater on GR/PPy-30 evaporator.

concentrations after evaporation and collection completely meet the WHO standards of potable water [66]. Removal efficiency of oil-water emulsion as shown in the Fig. S10, in the original solution, many oil droplets can be seen but no obvious oil droplets appeared in the distilled water. The treatment capacity of GR/PPy-30 aerogel for water sources contaminated with different organic compounds (dyes, antibiotics or VOCs) was tested by photothermal evaporation degradation synergistic experiment (photothermal water purification). The evaporation degradation process was shown in Fig. S11, GR/PPy-30 aerogel float naturally on the liquid surface and cover an elliptical collector. Under illumination, vapor can be effectively collected in the upper part of the collector and pollutants can be degraded by photocatalytic degradation in GR/PPy-30 aerogel. As shown in Fig. 8d, during evaporative degradation through the GR/PPy-30 aerogel, after 60 min treatment of MO solution, the MO characteristic peaks of residual solution and distilled water almost disappear compared with the initial solution and the calculated residual rate of MO is only 2.21% and 0.8% in residual solution and distilled water, respectively (Fig. 8e). Additionally, the same method was used to investigate the photothermal water purification capacity of aerogels in wastewater containing antibiotics such as ciprofloxacin (CIP). The residual rate of CIP is only 22.9% and 0.4% in residual solution and distilled water, respectively (Fig. 8f). Hence, the GR/PPy-30 aerogel can efficiently remove the pollutants in water while obtain clean distilled water. Due to the volatility at high temperature of phenol, the above evaporation device will increase the local temperature of the GR/PPy-30 aerogel, which will greatly increase the phenol content in the distilled water. Therefore, a self-made evaporation device is used here for the evaporation purification of phenol contaminated

water wastewater, as shown in Fig. S12. The device used low thermal conductivity commercially degreasing cotton and polystyrene foam to suppress the heat conduction loss and condensed water was adopted to reduce system temperature and prevent the evaporation of phenol. Fig. 8g shows the absorbance of phenol in the distilled water collected in different ways. The absorbance of distilled water collected directly without photothermal evaporation material and evaporated by GA are much higher than that of GR/PPy-30 aerogel materials and original solution with concentration of 20 mg L⁻¹. The corresponding concentrations were 41.54 mg L⁻¹ and 29.48 mg L⁻¹, which are 207.5% and 147.4% of the original solution, respectively (Fig. 8h), illustrating the enrichment of phenol in the distilled water through conventional photothermal evaporation. Hence, phenol in wastewater cannot be removed through solar photothermal driven phase transfer process. However, due to the superior photothermal evaporation and photocatalytic performance of GR/PPy-30, it can degrade phenol through solar-driven mass transfer and photocatalytic effect. It can be seen that the phenol content in the distilled water produced by evaporation of GR/PPy-30 aerogel is much lower than that of original solution and the distilled water obtained by other methods. The concentration of phenol in distilled water is 1.04 mg L⁻¹, illustrating the removal efficiency of phenol reaches 94.8%. Furthermore, complex wastewater respectively contained 10 mg L⁻¹ different pollutants including MO, RhB, CIP and phenol was used to measure the water purification capacity of GR/PPy-30 (Fig. 8i). It can be seen that the removal efficiency of different organic pollutants both reached above 90.0% in distilled water, suggesting the superior solar-driven water purification capacity of GR/PPy-30. Besides, the removal efficiency of different concentrations of VOCs has been

evaluated to prove the outstanding solar-driven water purification performance of GR/PPy-30 aerogel (Fig. S13). The results showed that in different concentration phenol solution, the removal efficiency in distilled water both reached above 90.0%, indicating the high removal efficiency of GR/PPy-30 towards VOCs pollutants via solar-driven water evaporation and photocatalytic capability.

The removal mechanism of VOCs wastewater can be illustrated by Fig. 9. The high optical absorption efficiency and porous structure of aerogel can effectively increase the refraction of light to increase the photothermal conversion efficiency. In addition, high specific surface area provided by porous structure can effectively improve water transport efficiency so that pollutants can be effectively transported to active sites of aerogel. This was confirmed by calculating the binding energy of PPy with water and phenol through DFT simulation calculation (Fig. 9a). Simulation results showed the binding energy of GR/PPy with water and phenol was -19.65 and -21.33 kJ mol $^{-1}$, respectively, which indicates that GR/PPy possesses a stronger binding ability to phenol due to the π - π conjugated structure between GR/PPy and phenol. Hence, in the process of photothermal evaporation, phenol is easier to combine with PPy and to be degraded, while water molecules are converted into steam easily through photothermal effect to evaporate. Besides, in the subsequent photocatalytic process, the photocatalysis mechanism of GR/PPy-30 was proposed and shown in Fig. 9b. The abundant porous structure of porous graphene nanosheets and the introduction of PPy endow aerogel with large specific surface area. The π - π interaction of PPy and graphene can effectively reduce the competitive adsorption of water and increase the adsorption performance for organic pollutants [67]. In addition, the abundant pore structure of aerogel can effectively adsorb pollutants into the active sites of catalyst. When GR/PPy-30 illuminated under simulated sunlight irradiation, it can effectively absorb most of the solar light sources and carry out photoexcitation effect, the following reaction occur between GR and PPy: [68]



in this progress, the electrons (e^-) in highest occupied molecular orbital (HOMO) of PPy will absorb photons and transform into excited states to migrate to the lowest unoccupied molecular orbital (LUMO) due to the $\pi \rightarrow \pi^*$ transition caused by high delocalization of PPy electrons. Meantime, due to the quick charge transfer effect of GR, the excited electrons will be migrated onto the surface of GR rapidly and further transfer to the aerogel surface to react with O_2 to form reactive oxygen species (ROS) such as $\cdot\text{O}_2^-$, thereby reacting with other groups through a series of chain reactions. In addition, the remaining holes (h^+) in LUMO can directly react with pollutants adsorbed on the surface. In general, a considerable number of electrons and holes will be reorganized in the photocatalytic process and lose their due role, with only a small number of electrons and holes involved in subsequent redox reactions, resulting in low quantum efficiency. However, the existence of GR could effectively inhibit the rapid recombination of electron-hole pairs due to the migration effect of GR on electrons, which extend the lifetime of photogenerated carriers. Therefore, GR/PPy aerogel have high quantum efficiency and can effectively remove organic pollutants under simulated sunlight. Thus, combine excellent photocatalytic and photothermal evaporation properties, aerogel can produce clean water effectively from wastewater by photothermal evaporation degradation.

4. Conclusions

In conclusion, we reported a holey GR/PPy aerogel with superior solar-driven water evaporation and photocatalysis performance, which could product clean water from different wastewater, especially VOCs contaminated water. The porous structure of GR/PPy aerogel could not only enhance the water transport, but also make the pollutants contact with photocatalytic activity sites more easily. The introduction of PPy

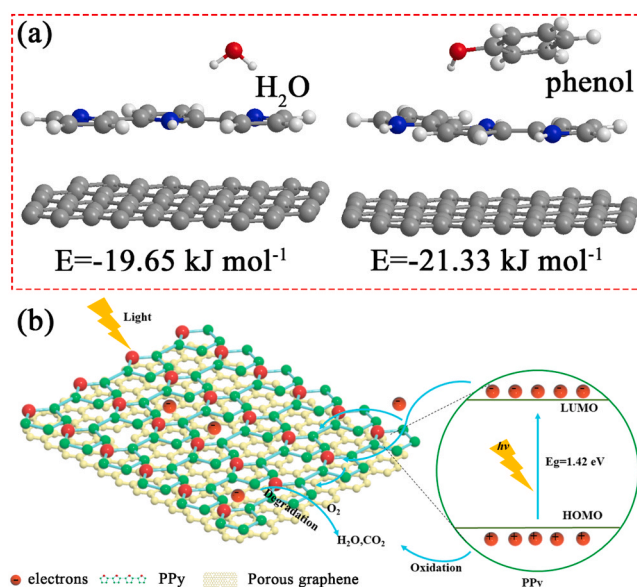


Fig. 9. Schematic diagram of employing the GR/PPy-30 aerogel evaporator for solar-driven water purification: (a) the binding energy of water and phenol with PPy, respectively; (b) overall photocatalysis mechanism of GR/PPy-30 aerogel.

avoids the agglomeration of RGO sheets, forming 3D self-supporting porous structure. Meanwhile, PPy endows aerogels high light absorption and the generation of photogenerated electrons capacity, which exhibit efficient solar-driven water evaporation and excellent photocatalysis capacity. The GR/PPy-30 aerogel can produce clean water via solar-driven water evaporation with an evaporation rate of 2.08 kg m $^{-2}$ h $^{-1}$ and energy conversion efficiency of $\sim 86.3\%$ under 1 sun irradiation. Thanks to this rational design, the GR/PPy-30 aerogel shows superior evaporation efficiency in different pollutants water sources and simultaneously degrades most pollutants through efficient photocatalysis. GR/PPy-30 aerogel shows excellent photocatalysis degradation efficiency for different organic pollutants such as dyes, VOCs and antibiotics, the degradation efficiency for RhB, phenol and CIP is up to 96.4, 92.5% and 82.6%, respectively. Furthermore, a phenol removal rate (94.8%) in distilled water is obtained during solar-driven water evaporation. Thus, the above results demonstrably suggest the solar-driven water purification of GR/PPy-30 aerogel combines the advantage of photocatalytic degradation and photothermal evaporation, which could obtain fresh water from complex water environment. Furthermore, the integration of photocatalytic degradation with photothermal evaporation could effectively expand the application of both technologies in the field of fresh water production to alleviate water shortage and environmental crisis.

CRediT authorship contribution statement

Shiwei Yan: Investigation, Software, Data curation, Writing – original draft. **Haojie Song:** Conceptualization, Supervision, Writing – review & editing, Funding acquisition. **Yong Li:** Supervision, Writing – review & editing, Funding acquisition. **Jin Yang:** Methodology, Validation. **Xiaohua Jia:** Project administration, Funding acquisition. **Sizhe Wang:** Resources, Formal analysis. **Xiaofei Yang:** Conceptualization, Supervision, Writing – review & editing, Funding acquisition.

Declaration of Competing Interest

The authors declare that they have no known competing financial interests or personal relationships that could have appeared to influence the work reported in this paper.

Acknowledgements

The authors acknowledge funding from National Natural Science Foundation of China (51875330, 51975342 and 21975129); Natural Science Foundation of Shaanxi Province (No. 2021JQ-553). China Postdoctoral Science Foundation (2020M673603XB) and Science Fund for Distinguished Young Scholars, Nanjing Forestry University (JC2019002).

Appendix A. Supporting information

Supplementary data associated with this article can be found in the online version at doi:10.1016/j.apcatb.2021.120820.

References

- [1] Z. Gao, H. Yang, J. Li, L. Kang, L. Wang, J. Wu, S. Guo, Simultaneous evaporation and decontamination of water on a novel membrane under simulated solar light irradiation, *Appl. Catal. B: Environ.* 267 (2020), 118695, <https://doi.org/10.1016/j.apcatb.2020.118695>.
- [2] Z. Zhou, X. Ma, D. Chen, X. Wan, X. Wan, Z. Fang, X. Peng, Polyaniline-coated MOFs nanorod arrays for efficient evaporation-driven electricity generation and solar steam desalination, *Adv. Sci.* 8 (2021), 2004552, <https://doi.org/10.1002/advs.202004552>.
- [3] D. Qi, Y. Liu, Y. Liu, Z. Liu, Y. Luo, H. Xu, X. Zhou, J. Zhang, H. Yang, W. Wang, X. Chen, Polymeric membranes with selective solution-diffusion for intercepting volatile organic compounds during solar-driven water remediation, *Adv. Mater.* 32 (2020), 2004401, <https://doi.org/10.1002/adma.202004401>.
- [4] Q. Ma, P. Yin, M. Zhao, Z. Luo, Y. Huang, Q. He, Y. Yu, Z. Liu, Z. Hu, B. Chen, H. Zhang, MOF-based hierarchical structures for solar-thermal clean water production, *Adv. Mater.* 31 (2019), 1808249, <https://doi.org/10.1002/adma.201808249>.
- [5] J. Zhou, Y. Gu, P. Liu, P. Wang, L. Miao, J. Liu, A. Wei, X. Mu, J. Li, J. Zhu, Development and evolution of the system structure for highly efficient solar steam generation from zero to three dimensions, *Adv. Funct. Mater.* 29 (2019), 1903255, <https://doi.org/10.1002/adfm.201903255>.
- [6] M. Wu, L. Li, Y. Xue, G. Xu, L. Tang, N. Liu, W. Huang, Fabrication of ternary GO/g-C₃N₄/MoS₂ flower-like heterojunctions with enhanced photocatalytic activity for water remediation, *Appl. Catal. B: Environ.* 228 (2018) 103–112, <https://doi.org/10.1016/j.apcatb.2018.01.063>.
- [7] K. Sekar, C. Chuaicham, B. Vellaichamy, W. Li, W. Zhuang, X. Lu, B. Ohtani, K. Sasaki, Cubic Cu₂O nanoparticles decorated on TiO₂ nanofiber heterostructure as an excellent synergistic photocatalyst for H₂ production and sulfamethoxazole degradation, *Appl. Catal. B: Environ.* 294 (2021), 120221, <https://doi.org/10.1016/j.apcatb.2021.120221>.
- [8] Q. Wu, J. Cao, X. Wang, Y. Liu, Y. Zhao, H. Wang, Y. Liu, H. Huang, F. Liao, M. Shao, Z. Shao, A metal-free photocatalyst for highly efficient hydrogen peroxide photoproduction in real seawater, *Nat. Commun.* 12 (2021) 483, <https://doi.org/10.1038/s41467-020-20823-8>.
- [9] P. Tao, G. Ni, C. Song, W. Shang, J. Wu, J. Zhu, G. Chen, T. Deng, Solar-driven interfacial evaporation, *Nat. Energy* 3 (2018) 1031–1041, <https://doi.org/10.1038/s41560-018-0260-7>.
- [10] L. Wu, Y. Ishigaki, Y. Hu, K. Sugimoto, W. Zeng, T. Harimoto, Y. Sun, J. He, T. Suzuki, X. Jiang, H. Chen, D. Ye, H₂S-activatable near-infrared afterglow luminescent probes for sensitive molecular imaging in vivo, *Nat. Commun.* 11 (2020) 446, <https://doi.org/10.1038/s41467-020-14307-y>.
- [11] Y. Wang, X. Wu, B. Shao, X. Yang, G. Owens, H. Xu, Boosting solar steam generation by structure enhanced energy management, *Sci. Bull.* 65 (2020) 1380–1388, <https://doi.org/10.1016/j.scib.2020.04.036>.
- [12] H. Wang, W. Xie, B. Yu, B. Qi, R. Liu, X. Zhuang, S. Liu, P. Liu, J. Duan, J. Zhou, Simultaneous solar steam and electricity generation from synergistic salinity-temperature gradient, *Adv. Energy Mater.* 11 (2021), 2100481, <https://doi.org/10.1002/aenm.202100481>.
- [13] Y. Lu, D. Fan, Y. Wang, H. Xu, C. Lu, X. Yang, Surface patterning of two-dimensional nanostructure-embedded photothermal hydrogels for high-yield solar steam generation, *ACS Nano* 15 (2021) 10366–10376, <https://doi.org/10.1021/acsnano.1c02578>.
- [14] Y. Wang, X. Wu, T. Gao, Y. Lu, X. Yang, G. Chen, G. Owens, H. Xu, Same materials, bigger output: a reversibly transformable ²D–³D photothermal evaporator for highly efficient solar steam generation, *Nano Energy* 79 (2021), 105477, <https://doi.org/10.1016/j.nanoen.2020.105477>.
- [15] L. Mascaretti, A. Schirato, R. Zboril, S. Kment, P. Schmuki, A. Alabastri, A. Naldoni, Solar steam generation on scalable ultrathin thermoplasmonic TiN nanocavity arrays, *Nano Energy* 83 (2021), 105828, <https://doi.org/10.1016/j.nanoen.2021.105828>.
- [16] B. Ge, S.W. Tang, H. Zhang, W.Z. Li, M. Wang, G. Ren, Z.Z. Zhang, Water vapor recovery device designed with interface local heating principle and its application in clean water production, *J. Mater. Chem. A* 9 (2021) 7967–7976, <https://doi.org/10.1039/D1TA00078K>.
- [17] X. Zhou, F. Zhao, Y. Guo, B. Rosenberger, G. Yu, Architecting highly hydratable polymer networks to tune the water state for solar water purification, *Sci. Adv.* 5 (2019) eaaw5484, <https://doi.org/10.1126/sciadv.aaw5484>.
- [18] L. Wu, Z. Dong, Z. Cai, T. Ganapathy, N. Fang, C. Li, C. Yu, Y. Zhang, Y. Song, Highly efficient three-dimensional solar evaporator for high salinity desalination by localized crystallization, *Nat. Commun.* 11 (2020) 521, <https://doi.org/10.1038/s41467-020-14366-1>.
- [19] X. Wu, Y. Wang, P. Wu, J. Zhao, Y. Lu, X. Yang, H. Xu, Dual-zone photothermal evaporator for antisalt accumulation and highly efficient solar steam generation, *Adv. Funct. Mater.* 31 (2021), 2102618, <https://doi.org/10.1002/adfm.202102618>.
- [20] Y. Kuang, C. Chen, S. He, E. Hitz, Y. Wang, W. Gan, R. Mi, L. Hu, A high-performance self-regenerating solar evaporator for continuous water desalination, *Adv. Mater.* 31 (2019), 1900498, <https://doi.org/10.1002/adma.201900498>.
- [21] F. Zhao, X. Zhou, Y. Shi, X. Qian, M. Alexander, X. Zhao, S. Mendez, R. Yang, L. Qu, G. Yu, Highly efficient solar vapour generation via hierarchically nanostructured gels, *Nat. Nanotechnol.* 13 (2018) 489–495, <https://doi.org/10.1038/s41565-018-0097-z>.
- [22] L. Shi, Y. Shi, S. Zhou, C. Zhang, Y. Aldrees, S. Aleid, P. Wang, Multi-functional 3D honeycomb ceramic plate for clean water production by heterogeneous photo-Fenton reaction and solar-driven water evaporation, *Nano Energy* 60 (2019) 222–230, <https://doi.org/10.1016/j.nanoen.2019.03.039>.
- [23] H. Song, Y. Liu, Z. Liu, M. Singer, C. Li, A. Cheney, D. Ji, L. Zhou, N. Zhang, X. Zeng, Z. Bei, Z. Yu, S. Jiang, Q. Gan, Cold vapor generation beyond the input solar energy limit, *Adv. Sci.* 5 (2018), 1800222, <https://doi.org/10.1002/advs.201800222>.
- [24] X. Li, J. Li, J. Lu, N. Xu, C. Chen, X. Min, B. Zhu, H. Li, L. Zhou, S. Zhu, T. Zhang, J. Zhu, Enhancement of interfacial solar vapor generation by environmental energy, *Joule* 2 (2018) 1331–1338, <https://doi.org/10.1016/j.joule.2018.04.004>.
- [25] S. Yan, Y. Li, F. Xie, J. Wu, X. Jia, J. Yang, H. Song, Z. Zhang, Environmentally safe and porous MS@TiO₂@PPy monoliths with superior visible-light photocatalytic properties for rapid oil-water separation and water purification, *ACS Sustain. Chem. Eng.* 8 (2020) 5347–5359, <https://doi.org/10.1021/acssuschemeng.0c00360>.
- [26] C. Mu, Y. Zhang, W. Cui, Y. Liang, Y. Zhu, Removal of bisphenol A over a separation free 3D Ag₃PO₄-graphene hydrogel via an adsorption-photocatalysis synergy, *Appl. Catal. B: Environ.* 212 (2017) 41–49, <https://doi.org/10.1016/j.apcatb.2017.04.018>.
- [27] C. Dai, B. Liu, Conjugated polymers for visible-light-driven photocatalysis, *Energy Environ. Sci.* 13 (2020) 24–52, <https://doi.org/10.1039/C9EE01935A>.
- [28] S. Zhang, J. Yi, J. Chen, Z. Yin, T. Tang, W. Wei, S. Cao, H. Xu, Spatially confined Fe₂O₃ in hierarchical SiO₂@TiO₂ hollow sphere exhibiting superior photocatalytic efficiency for degrading antibiotics, *Chem. Eng. J.* 380 (2020), 122583, <https://doi.org/10.1016/j.cej.2019.122583>.
- [29] S. Yu, Y. Wang, F. Sun, R. Wang, Y. Zhou, Novel mpg-C₃N₄/TiO₂ nanocomposite photocatalytic membrane reactor for sulfamethoxazole photodegradation, *Chem. Eng. J.* 337 (2018) 183–192, <https://doi.org/10.1016/j.cej.2017.12.093>.
- [30] T. Liu, L. Finn, M. Yu, H. Wang, T. Zhai, X. Lu, Y. Tong, Y. Li, Polyaniline and polypyrrole pseudocapacitor electrodes with excellent cycling stability, *Nano Lett.* 14 (2014) 2522–2527, <https://doi.org/10.1021/nl500255v>.
- [31] X. Yuan, D. Floresyona, P. Aubert, T. Bui, S. Remita, S. Ghosh, F. Brisset, F. Goubard, H. Remita, Photocatalytic degradation of organic pollutant with polypyrrole nanostructures under UV and visible light, *Appl. Catal. B: Environ.* 242 (2019) 284–292, <https://doi.org/10.1016/j.apcatb.2018.10.002>.
- [32] C. Wei, X. Zhang, S. Ma, C. Zhang, Y. Li, D. Chen, H. Jiang, Z. Xu, X. Huang, Ultra-robust vertically aligned three-dimensional (3D) Janus hollow fiber membranes for interfacial solar-driven steam generation with salt-resistant and multi-media purification, *Chem. Eng. J.* 425 (2021), 130118, <https://doi.org/10.1016/j.cej.2021.130118>.
- [33] Y. Wu, L. Shen, C. Zhang, H. Gao, J. Chen, L. Jin, P. Lin, H. Zhang, Y. Xia, Polyacid doping-enabled efficient solar evaporation of polypyrrole hydrogel, *Desalination* 505 (2021), 114766, <https://doi.org/10.1016/j.desal.2020.114766>.
- [34] S. Dong, Y. Zhao, J. Yang, X. Liu, W. Li, L. Zhang, Y. Wu, J. Sun, J. Feng, Y. Zhu, Visible-light responsive PDI/rGO composite film for the photothermal catalytic degradation of antibiotic wastewater and interfacial water evaporation, *Appl. Catal. B: Environ.* 291 (2021), 120127, <https://doi.org/10.1016/j.apcatb.2021.120127>.
- [35] K. Lu, L. Yuan, X. Xin, Y. Xu, Hybridization of graphene oxide with commercial graphene for constructing 3D metal-free aerogel with enhanced photocatalysis, *Appl. Catal. B: Environ.* 226 (2018) 16–22, <https://doi.org/10.1016/j.apcatb.2017.12.032>.
- [36] K. Lu, X. Xin, N. Zhang, Z. Tang, Y. Xu, Photoredox catalysis over graphene aerogel-supported composites, *J. Mater. Chem. A* 6 (2018) 4590–4604, <https://doi.org/10.1039/C8TA00728D>.
- [37] Y. Xu, Z. Lin, X. Zhong, X. Huang, N. Weiss, Y. Huang, X. Duan, Holey graphene frameworks for highly efficient capacitive energy storage, *Nat. Commun.* 5 (2014) 4554, <https://doi.org/10.1038/ncomms5554>.
- [38] L. Tang, C. Jia, Y. Xue, L. Li, A. Wang, G. Xu, N. Liu, M. Wu, Fabrication of compressible and recyclable macroscopic g-C₃N₄/GO aerogel hybrids for visible-light harvesting: a promising strategy for water remediation, *Appl. Catal. B: Environ.* 217 (2017) 241–248.
- [39] G. Neelgund, V. Bliznyuk, A. Oki, Photocatalytic activity and NIR laser response of polyaniline conjugated graphene nanocomposite prepared by a novel acid-less method, *Appl. Catal. B: Environ.* 187 (2016) 357–366, <https://doi.org/10.1016/j.apcatb.2016.01.009>.

- [40] M. Wang, X. Duan, Y. Xu, X. Duan, Functional three-dimensional graphene/polymer composites, *ACS Nano* 10 (2016) 7231–7247, <https://doi.org/10.1021/acsnano.6b03349>.
- [41] D. Marcano, D. Kosynkin, J. Berlin, J. Tour, Improved synthesis of graphene oxide, *ACS Nano* 4 (2010) 4806–4814, <https://doi.org/10.1021/nn1006368>.
- [42] M. Kim, C. Lee, Y. Seo, S. Cho, J. Kim, G. Lee, Y. Kim, J. Jang, Fabrication of various conducting polymers using graphene oxide as a chemical oxidant, *Chem. Mater.* 27 (2015) 6238–6248, <https://doi.org/10.1021/acs.chemmater.5b01408>.
- [43] Y. Xu, Z. Lin, X. Zhong, X. Huang, N. Weiss, Y. Huang, X. Duan, Holey graphene frameworks for highly efficient capacitive energy storage, *Nat. Commun.* 5 (2014) 4554, <https://doi.org/10.1038/ncomms5554>.
- [44] Z. Fan, J. Zhu, X. Sun, Z. Cheng, Y. Liu, Y. Wang, High density of free-standing holey graphene/PPy films for superior volumetric capacitance of supercapacitors, *ACS Appl. Mater. Interfaces* 9 (2017) 21763–21772, <https://doi.org/10.1021/acscami.7b03477>.
- [45] T. Liu, L. Zhang, B. Cheng, X. Hu, J. Yu, Holey graphene for electrochemical energy storage, *Cell Rep. Phys. Sci.* 1 (2020), 100215, <https://doi.org/10.1016/j.xcrp.2020.100215>.
- [46] J. Zhang, S. Wang, M. Xu, Y. Wang, H. Xia, S. Zhang, X. Guo, S. Wu, Polypyrrole-coated SnO₂ hollow spheres and their application for ammonia sensor, *J. Phys. Chem. C* 113 (2009) 1662–1665.
- [47] J. Zhong, S. Gao, G. Xue, B. Wang, Study on enhancement mechanism of conductivity induced by graphene oxide for polypyrrole nanocomposites, *Macromolecules* 48 (2015) 1592–1597, <https://doi.org/10.1021/jp8096633>.
- [48] Y. Han, T. Wang, T. Li, X. Gao, W. Li, Z. Zhang, Y. Wang, X. Zhang, Preparation and electrochemical performances of graphene/polypyrrole nanocomposite with anthraquinone-graphene oxide as active oxidant, *Carbon* 119 (2017) 111–118, <https://doi.org/10.1016/j.carbon.2017.04.030>.
- [49] Y. Wang, J. Yang, L. Wang, K. Du, Q. Yin, Q. Yin, Polypyrrole/graphene/polyaniline ternary nanocomposite with high thermoelectric power factor, *ACS Appl. Mater. Interfaces* 9 (2017) 20124–20131.
- [50] R. Wang, K. Lu, F. Zhang, Z. Tang, Y. Xu, 3D carbon quantum dots/graphene aerogel as a metal-free catalyst for enhanced photosensitization efficiency, *Appl. Catal. B: Environ.* 233 (2018) 11–18, <https://doi.org/10.1016/j.apcatb.2018.03.108>.
- [51] S. Pei, H. Cheng, The reduction of graphene oxide, *Carbon* 50 (2012) 3210–3228, <https://doi.org/10.1016/j.carbon.2011.11.010>.
- [52] L. Jiang, J. Syed, G. Zhang, Y. Ma, J. Ma, H. Lu, X. Meng, Enhanced anticorrosion performance of PPY-graphene oxide/PPY-camphorsulfonic acid composite coating for 304SS bipolar plates in proton exchange membrane fuel cell, *J. Ind. Eng. Chem.* 80 (2019) 497–507, <https://doi.org/10.1016/j.jiec.2019.08.032>.
- [53] A. Moysewicz, G. Gryglewicz, High-performance hybrid capacitor based on a porous polypyrrole/reduced graphene oxide composite and a redox-active electrolyte, *Electrochim. Acta* 354 (2020), 136661, <https://doi.org/10.1016/j.electacta.2020.136661>.
- [54] S. Golczak, A. Kancierzewska, M. Fahlman, K. Langer, J. Langer, Comparative XPS surface study of polyaniline thin films, *Solid State Ion.* 179 (2008) 2234–2239, <https://doi.org/10.1016/j.ssi.2008.08.004>.
- [55] R. Rajagopalan, J. Iroh, Characterization of polyaniline–polypyrrole composite coatings on low carbon steel: a XPS and infrared spectroscopy study, *Appl. Surf. Sci.* 218 (2003) 58–69, [https://doi.org/10.1016/S0169-4332\(03\)00579-8](https://doi.org/10.1016/S0169-4332(03)00579-8).
- [56] L. Ruangchuay, J. Schwank, A. Sirivat, Surface degradation of α -naphthalene sulfonate-doped polypyrrole during XPS characterization, *Appl. Surf. Sci.* 199 (2002) 128–137, [https://doi.org/10.1016/S0169-4332\(02\)00564-0](https://doi.org/10.1016/S0169-4332(02)00564-0).
- [57] W. Zhang, C. Shen, G. Lu, Y. Ni, C. Lu, Z. Xu, Synthesis of PPy/RGO-based hierarchical material with super-paramagnetic behavior and understanding its robust photo current driven by visible light, *Synth. Met.* 241 (2018) 17–25, <https://doi.org/10.1016/j.synthmet.2018.03.018>.
- [58] Y. Zhao, J. Liu, Y. Hu, H. Cheng, C. Hu, C. Jiang, L. Jiang, A. Cao, L. Qu, Highly compression-tolerant supercapacitor based on polypyrrole-mediated graphene foam electrodes, *Adv. Mater.* 25 (2013) 591–595.
- [59] Z. Fan, J. Zhu, X. Sun, Z. Cheng, Y. Liu, Y. Wang, High density of free-standing holey graphene/PPy films for superior volumetric capacitance of supercapacitors, *ACS Appl. Mater. Interfaces* 9 (2017) 21763–21772.
- [60] C. Li, Z.Y. Wu, H.W. Liang, J.F. Chen, S.H. Yu, Ultralight multifunctional carbon-based aerogels by combining graphene oxide and bacterial cellulose, *Small* 13 (2017), 1700453, <https://doi.org/10.1002/smll.201700453>.
- [61] Y. Zhao, J. He, Hierarchically porous rGO synthesized by microwave reduction propagation for highly efficient adsorption and enrichment of lindane, *Colloids Surf. A: Physicochem. Eng. Asp.* 626 (2021), 127017.
- [62] Y. Li, S. Yan, X. Jia, J. Wu, J. Yang, C. Zhao, S. Wang, H. Song, X. Yang, Uncovering the origin of full-spectrum visible-light-responsive polypyrrole supramolecular photocatalysts, *Appl. Catal. B: Environ.* 287 (2021), 119926, <https://doi.org/10.1016/j.apcatb.2021.119926>.
- [63] W. Zhao, J. Li, T. She, S. Ma, Z. Cheng, G. Wang, P. Zhao, W. Wei, D. Xiao, D. Leung, Study on the photocatalysis mechanism of the Z-scheme cobalt oxide nanocubes/carbon nitride nanosheets heterojunction photocatalyst with high photocatalytic performances, *J. Hazard. Mater.* 402 (2021), 123839, <https://doi.org/10.1016/j.jhazmat.2020.123839>.
- [64] L. Yang, X. Bai, J. Shi, X. Du, L. Xu, P. Jin, Quasi-full-visible-light absorption by D35-TiO₂/g-C₃N₄ for synergistic persulfate activation towards efficient photodegradation of micropollutants, *Appl. Catal. B: Environ.* 256 (2019), 117759, <https://doi.org/10.1016/j.apcatb.2019.117759>.
- [65] F. Chen, W. An, L. Liu, Y. Liang, W. Cui, Highly efficient removal of bisphenol A by a three-dimensional graphene hydrogel-AgBr@rGO exhibiting adsorption/photocatalysis synergy, *Appl. Catal. B: Environ.* 217 (2017) 65–80, <https://doi.org/10.1016/j.apcatb.2017.05.078>.
- [66] D. Qi, Y. Liu, Y. Liu, Z. Liu, Y. Luo, H. Xu, X. Zhou, J. Zhang, H. Yang, W. Wang, X. Chen, Polymeric membranes with selective solution-diffusion for intercepting volatile organic compounds during solar-driven water remediation, *Adv. Mater.* 32 (2020), 2004401, <https://doi.org/10.1002/adma.202004401>.
- [67] Y. Li, W. Cui, L. Liu, R. Zong, W. Yao, Y. Liang, Y. Zhu, Removal of Cr(VI) by 3D TiO₂-graphene hydrogel via adsorption enriched with photocatalytic reduction, *Appl. Catal. B: Environ.* 199 (2016) 412–423, <https://doi.org/10.1016/j.apcatb.2016.06.053>.
- [68] H. Noreen, J. Iqbal, A. Arshad, R. Faryal, Ata-ur-Rahman, R. Khattak, Sunlight induced catalytic degradation of bromophenol blue and antibacterial performance of graphene nanoplatelets/polypyrrole nanocomposites, *J. Solid State Chem.* 275 (2019) 141–148, <https://doi.org/10.1016/j.jssc.2019.03.045>.